Article

Ultra-low power-consumption OLEDs via phosphor-assisted thermally-activated-delayed-fluorescence-sensitized narrowband emission

Chen Yin[1,4], Yangyang Xin[1,4], Tianyu Huang[1], Qisheng Zhang [2], Lian Duan [1,3] & Dongdong Zhang [1] ✉

The further success of OLED beyond conventional low-luminance display applications has been hampered by the low power efficiency (PE) at high luminance. Here, we demonstrate the strategic implementation of an exceptionally high-PE, high-luminance OLED using a phosphor-assisted thermally-activated-delayed-fluorescence (TADF)-sensitized narrowband emission. On the basis of a TADF sensitizing-host possessing a fast reverse intersystem crossing, an anti-aggregation-caused-quenching character and a good bipolar charge-transporting ability, this design achieves not only a 100% exciton radiative consumption with decay times mainly in the sub-microsecond regime to mitigate exciton annihilations for nearly roll-off-free external quantum efficiency, but also narrowband emission with both small energetic loss during energy transfer and resistive loss with increasing luminance. Consequently, besides a maximum PE of 187.7 lm/W, an exceptionally high critical maximum luminance (where a PE of 100 lm/W is maintained) of over 110,000 cd/m² is achieved for the proof-of-the-concept device, nearly one-of-magnitude higher than the previous record.

The development of low-power electronic displays has become a long-term goal for future global sustainable development, as artificial lighting and displays consume >20% of the world's electricity. Currently, liquid crystal displays (LCDs) are the dominant technology, with applications ranging from smartphones, tablets, computer monitors, televisions to data projectors. However, LCDs are non-emissive and need a white light-emitting diode for backlighting, which would suffer from a narrow color gamut and increase power consumption as well. In comparison, the latest display technology, organic light emitting diodes (OLEDs), uses emissive pixels directly without an external backlight, inherently favoring a low power consumption[1–3]. Combining with several other advantages, including true black, fast response time, and an ultra-thin profile that enables flexible shapes, the market for OLED displays has grown rapidly, challenging LCDs in all applications, especially in high-end and mid-range smartphones.

Of all the parameters that measure the nature of OLEDs, power efficiency (PE), defined as the specific ratio of luminous flux (in lumens) to the electrical power input (in watts) by the device, directly describes how well a display or lighting application could reduce power consumption[4]. The breakthrough to high PEs has been achieved by using phosphorescence and thermally activated delayed fluorescence (TADF) emitters, which can harness all excitons formed

[1]Key Laboratory of Organic Optoelectronics and Molecular Engineering of Ministry of Education, Department of Chemistry, Department of Chemistry, Tsinghua University, Beijing, China. [2]MOE Key Laboratory of Macromolecular Synthesis and Functionalization, Department of Polymer Science and Engineering, Zhejiang University, Hangzhou, China. [3]Laboratory of Flexible Electronics Technology, Tsinghua University, Beijing, China. [4]These authors contributed equally: Chen Yin, Yangyang Xin. ✉e-mail: ddzhang@mail.tsinghua.edu.cn

under electrical excitation and convert them into photons[5–8]. OLEDs with maximum PEs (PE$_{max}$s) in excess of 100 lm/W, therefore, have been widely reported (usually at relatively low luminance levels of <1000 cd/m^2), and a record of over 200 lm/W has been achieved without additional light extraction techniques[4,9–26]. As a result, OLED technology has reached a certain level of maturity in terms of efficiency and stability in application scenarios where relatively low luminance (<5000 cd/m^2) is required, such as smartphone displays. However, a notorious problem with OLEDs remains unresolved, namely the tendency for efficiency to decrease with increasing luminance, known as efficiency roll-off, and in particular PE[27]. To illustrate the PE roll-off behavior of OLEDs, we define L$_{PE=100\ lm/W}$ as the critical luminance of a device at which a PE of 100 lm/W can be achieved. Figure 1a and Supplementary Table 1 summarize the relationship between PE$_{max}$ and L$_{PE=100\ lm/W}$ for the reported high-efficiency devices with PE$_{max}$ > 100 lm/W based on different types of emitters. It is clear that the majority of L$_{PE=100\ lm/W}$s are in the range of 500–5000 cd/m^2, with only one work so far able to achieve a value above 10,000 cd/m^2. Other non-commercial applications of OLED technology, which require much higher brightness levels (>10,000 cd/m^2), have been severely hampered by this clear exclusion of high PE and high luminance. Breaking this trade-off has been an urgent but challenging task for the OLED community.

Here, deriving from our previous work on phosphor-assisted TADF-sensitized fluorescence (pTSF)[28], we unveiled a breakthrough strategy for OLEDs to fully exploit the potential of a high PE under a high luminance, of which the implementation was on the basis of a multiple sensitized narrowband emission from a ternary components emitting layer constituting a TADF sensitizing-host, a phosphor-assistant and a multiple resonance (MR) emitter. This strategic design was able to achieve a 100% exciton radiative consumption with decay times mainly in the sub-microsecond regime, favoring the suppression of exciton annihilation under high brightness for nearly roll-off-free EQE. An ortho-linked donor-dual-acceptor architecture TADF molecule simultaneously possessing a fast reverse intersystem crossing (ISC), an anti-aggregation caused quenching character, a bipolar charge transport ability, and moderate energy levels was correspondingly developed, aiming to not only maximize the efficiency of pTSF emission, but also reduce the energetic and resistive losses incurred during electron-photon conversion with increasing luminance as well. The optimal pTSF device exhibited a narrowband electroluminescence (EL) spectrum with a small FWHM of 30 nm, a high external quantum efficiency of 33.3%, and a low operating voltage of 4.25 V recorded at 100,000 cd/m^2 simultaneously. A high J$_{90\%}$, which is defined as the current density at which the EQE falls to 90% of its peak value, of ~65 mA/cm^2 was observed, outperforming nearly all reported

OLEDs with EQE > 20%[29]. Moreover, the above operation voltage represents the lowest one among green OLEDs in literature, even comparable with or better than the cutting-edge perovskite LEDs and polaritonic OLEDs[30–32]. As a result, not only a large PE$_{max}$ of 187.7 lm/W was achieved, but also a truly remarkable high L$_{PE=100\ lm/W}$ of over 110,000 cd/m^2, almost one-of-magnitude higher than the previous record. Moreover, the fast radiative consumption of excitons also extended the operation lifetime of the device, realizing a long LT90 (time to 90% of the initial luminance) of 135 h at an initial luminance (L$_0$) of 10,000 cd/m^2. Our work here greatly relieved the critical issue of PE roll-off with increasing luminance and push the L$_{PE=100\ lm/W}$ up to a higher level, highlighting the potential for the continued success of OLEDs beyond conventional low luminance display applications.

Results

The design concept of large PE device at high luminance

In principle, PE is proportional to K$_r$E$_{Ph}$/e × EQE/V, where K$_r$ is the luminous efficiency of the radiation, E$_{Ph}$ is the average photon energy over the full spectral range, EQE is the external quantum efficiency and V is the applied voltage[33]. In theory, K$_r$E$_{Ph}$/e is closely related to the spectra, and according to Macadam's limit, a narrowband spectrum is more favorable for a high PE[34]. Therefore, in order to obtain a high PE at high luminance, a narrowband emission, a high EQE and a low V should be achieved simultaneously. However, this is quite challenging. Although a high maximum EQE has been achieved by using phosphorescence and TADF emitters, the efficiency roll-off in EQE with increasing luminance has puzzled researchers for decades. And taking into account the energy and resistance losses that occur during electron-photon conversion with increasing luminance, the PE roll-off is always more severe than that of EQE. Albeit the complex underlying physics, excitons involved bimolecular annihilations have been accepted as the main reason for EQE roll-off, which is highly related with the exciton concentrations[27]. Though enlarging the recombination zone could partially alleviate this issue, the intrinsic slow microsecond-scale radiative decays of both phosphorescence and TADF emitters would also pile up excitons under high luminance. Using a TADF molecule as a sensitizer for a final fluorescent emitter, termed TADF-sensitized fluorescence (TSF), has believed to be an effective way in accelerating exciton consumptions due to the additional rapid Förster energy transfer (FET) from sensitizer to emitter[35,36]. However, owing to the competition from the fast ISC process of the TADF sensitizer, the energy transfer in TSF would be a multi-time process, and long-delayed EL decay tails have been experimentally observed in previous works[37]. Therefore, though being alleviated compared with TADF device, the EQE roll-off of TSF device is still unsatisfied.
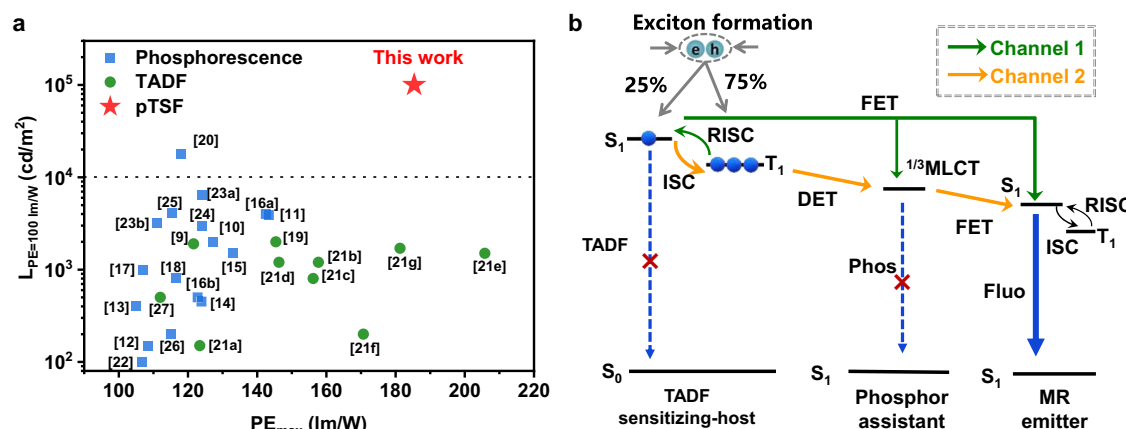

Fig. 1 | Summary of PEs and energy transfer process of pTSF. a The summarized PE$_{max}$ as a function of the critical luminance L$_{PE=100\ lm/W}$ of the previously reported devices. **b** The energy transfer diagram of the pTSF device constituting a TADF sensitizing host, a phosphor assistant and a MR narrowband emitter.

Fortunately, in our preliminary work, we proposed an advanced pTSF emission strategy, whereby a phosphor-assistant was introduced into TSF system[28]. Dual sensitization channels can be anticipated for pTSF, one being the FET process from singlet states of TADF sensitizing-host to that of the final emitter, another being the Dexter energy transfer from triplet states of TADF sensitizing-host to that of the phosphor and then to the singlet of the final emitter through a FET process. Different to multi-time FET processes in TSF system, the sensitization from phosphor to the final emitter is a one-way process, which thereafter greatly reduces the cycles numbers of the triplet ↔ singlet spin-flip transitions on TADF host induced by ISC process, thus eliminating the long EL decay tails in TSF system. As a consequence, pTSF devices could realize a 100% exciton utilization in a sub-microsecond-scale towards nearly free EQE roll-off. Nevertheless, towards a cutting-edge PE with alleviated efficiency roll-off, formidable challenges remain. To achieve an absolute PE value, not only a higher absolute EQE value is required, but also a narrowed EL spectrum bandwidth. Moreover, the wide-energy-gaps of TADF host and phosphor-assist required to guarantee efficiency energy transfer would inevitably cause energetic loss during the energy transfer to the low-energy-gap fluorophores. In terms of PE-roll-off, the adoption of wide-energy-gap host would also suffer from unbalanced and poor charge-carrier transport and inappropriate energy levels of the host that enlarge the interface barriers with the adjacent layers for charge injection, leading to the resistive loss reflected by the greatly enlarged operation voltage with increasing luminance, also causing severe PE roll-off.

With those in consideration, to unlock the full potential of PE performances on the basis of pTSF strategy, we constructed a narrowband pTSF emitting system consisting a TADF sensitizing-host, a phosphorescence-assistant and a MR emitter, as illustrated in Fig. 1b. The replacement of the final conventional fluorophore by a MR emitter could greatly enlarge the potential limitation of the absolute PE value because it could not only provide a narrowband spectrum for a high $K_r E_{Ph}/e$ value but also enlarge the absolute EQE value since the rigid planar structures of MR emitters prefer a horizontal emitting dipole moment orientation (EDO) to effectively enhance light outcoupling efficiency[38]. Besides, MR emitters are usually believed to be TADF molecules and thus possess the ability to harness triplet excitons themselves though being limited, thus favoring to block the exciton loss pathways through the dark triplet states faced by conventional fluorescence emitters. Last but not the least, owing to the small stokes shift of MR emitters, effectively transfer energy could be anticipated from TADF and phosphor sensitizers with E_gs being energetically-close to that of MR emitters, reducing the energetic loss during this transfer originated from their different energy gaps.

Besides the adoption of MR emitters, the TADF sensitizing-host is also crucial to maximize the PE performance of pTSF device as it not only affects the sensitization process but also influences the resistive loss. One essential requirement for TADF sensitizing host is a fast RISC constant, which is usually the rate-determining steps in sensitization system and hence affect the sensitization efficiency. Besides, an anti-aggregation-caused quenching (anti-ACQ) character should also be realized to suppress the potential exciton annihilations on host considering the fact that under high luminance, when the formation rate of excitons eventually exceeds their consumption rate, exciton saturation of dopants can be anticipated and thus excessive excitons on hosts[27]. In terms of reducing resistive loss, the TADF sensitizing host should simultaneously possess not only a good bipolar charge transporting ability but also suitable energy levels to match the adjacent transporting layers to reduce energy barrier. Interestingly, compared with conventional wide gap host with a large ΔE_{ST}, the donor-acceptor type TADF host with a small ΔE_{ST} would bear much smaller energy gap in the prerequisite of a same high triplet, which naturally favors orbital levels energetically-close to adjacent layers. Such characteristics of

TADF hosts have already been adopted to reduce the operation voltages in phosphorescence devices[20]. Based on the above discussion, by proper molecular design of TADF sensitizing host, pTSF device with a MR emitter have the great chance to realize a high PE at high luminance.

The design and characterization of TADF sensitizing host

Taking all the above mentioned requirements, 5,7-bis(3-(4,6-diphenyl-1,3,5-triazin-2-yl)-[1,1'-biphenyl]-4-yl)-5,7-dihydroindolo[2,3-b]carbazole (DPT-IC) was constructed as a TADF-sensitizing host, of which the structure was provided in Fig. 2a. In this molecule, 5,7-dihydroindolo[2,3-b]carbazole (23bICz) and 2,4,6-triphenyl-1,3,5-triazine (TRZ) groups were chosen as the donor and acceptor segments, respectively, both of which possessed well-validated carrier transporting characters and moderate energy levels to match most transporting materials. Besides, this molecule adopts an ortho-linked acceptor-donor-acceptor architecture aiming to, on one hand, to induce highly twisted molecular configuration so that the intermolecular interaction can be weakened to guarantee the anti-ACQ character, which can be further enhanced by the additional substitution of phenyl motif at the meta-position of triazine. On the other hand, the ortho-linkage would intrigue both through-space and through-bond charge transfer (TSCT and TBCT) transitions, which can be doubled by two equivalent acceptors. Those multiple transitions channels favor the generation of quasi-degenerate excited states to enhance the spin-orbital coupling (SOC) for a fast RISC, which can be demonstrated below. This molecule design is clearly different with previous works based on dual donors, which only showed dual TBCT transitions and thus only quadrupolar charge-transfer (CT) states[39].

To verify the rationality of molecular design, the electronic properties of DPT-IC were studied for which the ground-state optimization was performed by density functional theory (DFT) and excited-state electronic analysis by time-dependent DFT (TD-DFT) with a B3LYP/6-31(G)* using Gaussian program. Theoretical simulation showed a highly twisted stereochemical structure of DPT-IC with two TRZ groups being separately located at each site of 23bICz plane with torsion angles of 62.7° and 63.1° were recorded between the 23bICz plane and the linker-phenyl rings, respectively. Besides, dihedral angles between the triazine and linker-phenyl rings of 37.5° and 38.8°, respectively, were also observed. Figure 2b provides the frontier molecular orbital distributions of DPT-IC, showing a dominantly location of the highest occupied molecular orbital (HOMO) on 23bICz segment with part extending to the linker phenyl rings between donor and acceptor. As for the lowest unoccupied molecular orbital (LUMO), it volved equivalent distribution on both TRZ rings. Negligible orbital overlap between HOMO and LUMO favors a small energy difference (ΔE_{ST}) of 0.051 eV obtained from the theoretical predicted energy levels of the lowest singlet (2.562 eV) and triplet (2.511 eV). It is noteworthy that degenerate energy levels of singlet and triplet states were obtained with four pair degenerated singlets (S_1-S_4) and triplets (T_1-T_4) and the energy difference between T_1 and S_4 being merely 0.122 eV.

The origine of those degenerate energy levels, the existence of TSCT transition was theoretically analyzed firstly. The intramolecular face-to-face D/A motif endows close atom packing with distances in the range of 2.84–3.52 Å, favoring through-space electronic interactions. The reduced density gradient (RDG) analysis of DPT-IC was performed and the RDG isosurface map was provided in Fig. 2c, revealing the presence of obvious intramolecular Van der Waals interaction as indicated by the green regions between ICZ donor and TRZ acceptor units. The RDG scatter diagrams also validated this enhanced weak interactions in the region that Sign $(\lambda_2)\rho$ is near 0 (red square). Those results clear validated the existence of TSCT transition in DPT-IC and the ratios of TBCT and TSCT transitions can be obtained using a reported method, being 32% and 68%, respectively[40]. Afterwards, the hole-particle analysis of those states was also conducted
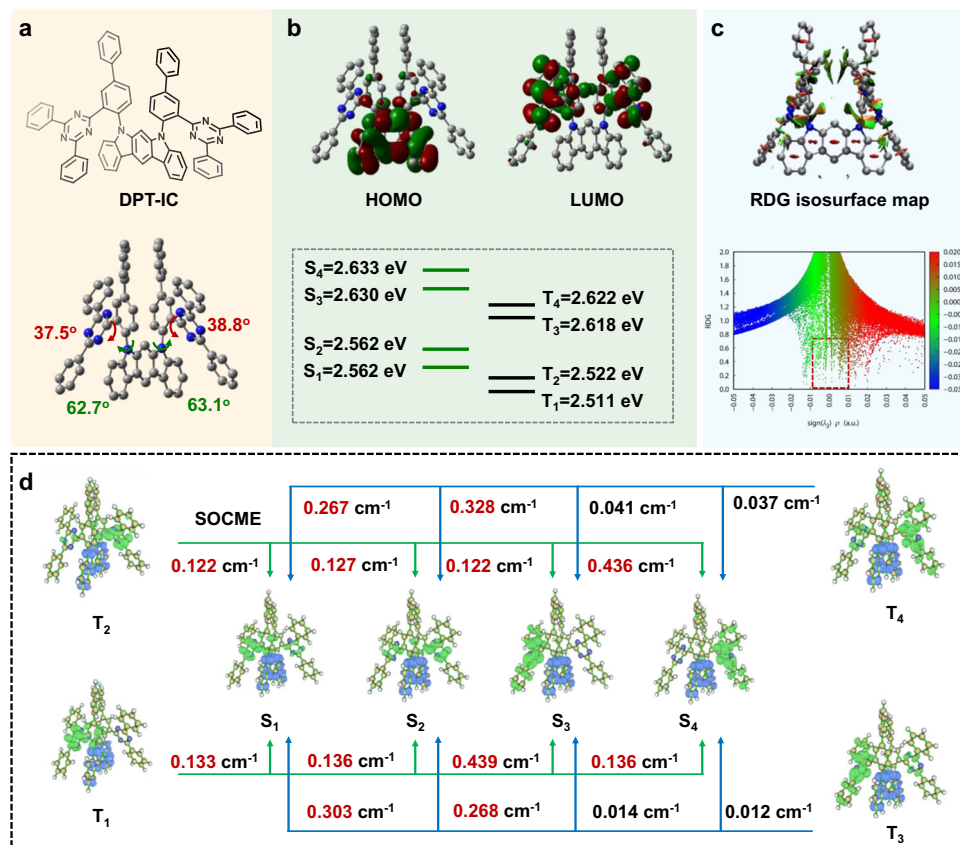
Fig. 2 | Theoretical calculations of DPT-IC. a The molecular structure and the optimized structural configuration; **b** the HOMO and LUMO distributions of DPT-IC and the degenerate energy levels; **c** The RGD isosuface map and the RDG scatter diagram of DPT-IC; **d** The hole-particle analysis of the degenerate states and their SOCEM constants.

and provided in Fig. 2d. Interestingly, S_1/T_1 and S_2/T_2 showed clear characteristics of hybrid localized (LE) and CT excited states, being TBCT transitions, while S_3/T_3 and S_4/T_4 exhibited totally CT type orbital distributions, being TSCT transitions. This demonstrated our inspirations that the molecule with orthro-linked dual-acceptor could induce multiple CT transition channels for degenerate energy levels. The spin-orbital coupling matrix element (SOCME) values between those degenerate states were also calculated with Orca. The SOCME constants between T_1 and S_3, T_2 and S_4, T_3 and S_1 as well as T_4 and S_2 are all even over 0.3 cm^{-1}, which are remarkable for organic TADF based on only carbon, hydrogen, and nitrogen atoms. And the SOC values between TBCT triplets and TSCT singlets or TBCT singlets and TSCT triplets are much larger than those of singlet and triplet states of TBCT or TSCT only. This is inconsistence with the El-sayed rules, that orbitals with different nature favors the spin-flip transitions. Though the underlying physics is debating, a second-order vibronic-coupling mechanism has been well recognized for RISC process in TADF molecules, whereby multiple states with different nature would mix with each other to mediate the RISC process. The degenerate energy levels of DPT-IC should therefore favor a fast RISC process theoretically.

The molecular synthesis procedure of DPT-IC was provided in Supplementary Fig. 1 and a high yield of ~86% was obtained using a classical C-N coupling. The molecular structure was detaily characterized by H^1 NMR, mass spectra and elemental analysis as provided in the Supporting Information (Supplementary Figs. 2, 3). Its single crystal structure was also determined by X-ray diffraction as provide in Supplementary Fig. 4. As expected, a highly twisted structure was observed with the two TRZ segments being localized at the different

sides of 23bICz group as predicted in the theoretical result. The torsion angles between the linker-phenyl rings and the 23bICz plane as well as the triazine rings were observed to be 58.16° and 72.58° as well as 26.65° and 26.28°, respectively. The twisted structure prevented the molecular interactions as expected. Analysis of thermal stability of DPT-IC was studied with thermogravimetric analysis (TGA) as depicted in Supplementary Fig. 5a. A high degradation temperature (at which the weight loss achieves 5 wt%) of 408 °C is recorded, rationalizing the employment of DPT-IC as a host for evaporation process. A large glass transition temperature (Tg) of 235 °C was also observed from differential scanning calorimetry (DSC) measurement (Supplementary Fig. 5b), benefiting from its twisted structures. The electrochemical properties of DPT-IC were studied by cyclic voltammetry (Supplementary Fig. 6), showing reversible reduction and qusi-reversible oxidation processes, suggesting both stable radical anions and cations. Moreover, moderate HOMO and LUMO energy levels of −2.7 eV and −5.8 eV were also obtained, which can well match the energy levels of the most adopted charge transporting materials. In addition to the intrinsic electronic properties of donor and acceptor moieties, those moderate energy levels also benefit from the small ΔE_{ST} of DPT-IC considering its high triplet levels.

Photophysical properties of DPT-IC and the doped films
Photophysical characterizations of DPT-IC were performed to further evaluate the rationality of molecular designing strategy. Ultraviolet-visible absorption (Abs), fluorescence (Fluo) and phosphorescence (Phos) spectra were measured in dilute toluene and given in Fig. 3a. From the Abs-spectrum, the absorption peaks at ~305 and ~362 nm can be assigned to the n-π* and π-π* transitions of 23bICz donor itself,
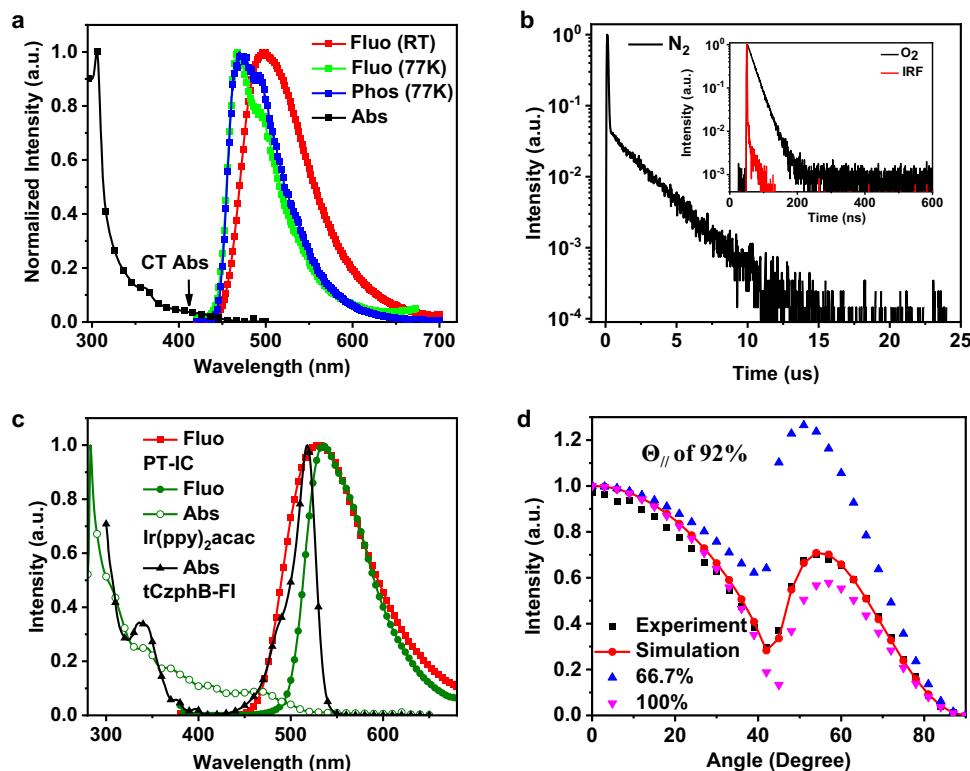
Fig. 3 | Photophysical characterizations. a UV-vis absorption, fluorescence and phosphorescence spectra of DPT-IC in toluene solution; **b** Photoluminescence transient decay curves of DPT-IC in toluene after bubbling nitrogen and oxygen (the inserted one); **c** The absorption spectra of Ir(ppy)₂acac and tCzphB-Fl as well as the emission spectra of DPT-IC pristine film and DPT-IC: 10 wt% Ir(ppy)₂acac; **d** The angle dependent PL spectrum of tCzphB-Fl in the doped film.

respectively, in agreement with the results of 23bICz segment measured in toluene (Supplementary Fig. 7). As for the wide and weak absorption peak around 420 nm, it was believed to originate from the CT transition from donor to acceptor. Owing to the weak oscillator strength of TSCT transition, this CT absorption intensity is weakened, similar to other TADF molecules with TSCT transitions[41]. Besides, wide and structureless Fluo-spectrum was recorded at room temperature (RT), showing an emission maximum at 505 nm in corresponding with the characteristic of a CT radiative transition. The Fluo-spectrum at 77 k was also recorded and showed a blue-shifted onset compared with the one at RT, which should be ascribed to the fixed molecular structure and the decreased environmental polarity in frozen toluene matrix[42]. The phosphorescence spectra in different solvents were also recorded at 77 k as illustrated in Supplementary Fig. 8a and though the solvatochromism was confirmed, the vibronic structure for phosphorescence spectrum obtained in toluene suggested a potentially mixed CT and LE character of DPT-IC triplet state. Moreover, the temperature-dependent decays in degassed toluene (Supplementary Fig. 8b) also validated the decreased TADF emission and the increased phosphorescence. The ΔE_{ST} of DPT-IC in toluene was finally obtained using S₁ (2.83 eV) and T₁ (2.80 eV) from the onset energies of the Fluo- and Phos-spectra at 77 k in toluene, respectively, being 0.03 eV.

The photoluminescence quantum yield (PLQY) and the transient decay behaviors before and after degassing were further performed to evaluate the TADF performances of DPT-IC, as illustrated in Fig. 3b and Supplementary Fig. 9. DPT-IC solution exhibited a low PLQY of only 0.21 before degassing, while a high value of near unity after degassing. Meanwhile, the decay curve after degassing showed a classic double-exponential characteristic with the fitted prompt and delayed lifetimes (τ_{PF} and τ_{DF}) of 38.4 ns and 2.2 μs, respectively. Those behaviors clearly validate the TADF property of DPT-IC. Based on those results, the corresponding rates of the radiative decay (k_r), RISC (k_{RISC}), and ISC

(k_{ISC}) can be calculated to be $5.5 \times 10^6\,s^{-1}$, $2.2 \times 10^6\,s^{-1}$ and $20.7 \times 10^6\,s^{-1}$, respectively. Though the high k_{RISC} should benefit from the degenerate energy levels from our molecular design, a fast ISC process with nearly ten-fold time larger was observed, which would compete with FET process in TSF channel as we discussed above. It should also be pointed that the k_{ISC} is also nearly four-fold time higher than k_r which increases the likelihood of exciton recycling between the singlet and triplet states rather than radiative decay. Fortunately, the highly twisted structure of DPT-IC increases the molecular rigidity and thus suppress the potential nonradiative decay to guarantee a high PLQY. The anti-ACQ performance of DPT-IC was further evaluated by being dispersed into 9-(3-(9H-carbazol-9-yl) phenyl)-9H-3,9'-bicarbazole (mCPBP) films with a gradient doping concentration. As a result, with the doping concentration of DPT-IC increasing from 10 wt% to 100 wt% (pristine film), the corresponding PLQY values only showed slight decrease from 94% to 78% (Supplementary Fig. 10), suggesting significant anti-ACQ property as we anticipated. The ΔE_{ST} of DPT-IC pristine film was obtained from the energy difference between its fluorescence and phosoresce spectra provided in Supplementary Fig. 11a, being 0.01 eV. Combining the transient decay behavior in Supplementary Fig. 11b, the kinetic rates of TADF process of DPT-IC pristine film can be calculated as provided in Supplementary Table 2, with k_r, k_{RISC}, and k_{ISC} being 1.1×10^7, 1.4×10^6 and $1.2 \times 10^7\,s^{-1}$, respectively.

To construct efficient pTSF film, the phosphor-assistant and the emitter should be finely chosen. In this work, bis[2-(2-pyridinyl-N)phenyl-C](acetylacetonato)iridium(III) [Ir(ppy)₂(acac)] was chosen as the phosphor-assistant while 2',5',11',14'-tetra-tert-butyl-3a2',8a2'-diaza-15b'-boradispiro[fluorene-9,7'-diacenaphtho[1,2,3,4-defg:1',2',3',4',5'-pqrst]pentaphene-9,9"-fluoren]-1',3',3a1'(15c'),3b', 4',6',7a',7a1'(15b1'),8a',9a', 9a1'(12a'),11',12b',12b1'(15a'),14'-pentadecaene (tCzphB-Fl) as the final MR emitter[43]. The related spectral information of involved molecules

was depicted in Fig. 3c. Significant spectral overlap can be verified between DPT-IC emission and Ir(ppy)$_2$acac/ tCzphB-FI absorption as well as between Ir(ppy)$_2$acac emission and tCzphB-FI absorption. With the corresponding photophysical properties, the corresponding FET radii can be calculated to be 3.9 and 2.5 nm from DPT-IC to 2tCzphB-FI and Ir(ppy)$_2$acac while 3.7 nm from Ir(ppy)$_2$acac to 2tCzphB-FI, respectively, all suggesting highly-efficient energy transfer. What deserves to be pointed out is that such large FET radii are obtained under the circumstance that the emission peaks of both TADF host and phosphor-assistant are only slightly blue-shifted compared with that of the MR emitter. Therefore, the energy loss during the energy transfer process could be reduced on the maximum degree, favoring a high PE value. The reason should be attributed to the small stokes shift of the MR emitter. The doped film of DPT-IC: 10 wt% Ir(ppy)$_2$acac: 1 wt% tCzphB-FI achieved a nearly unity PLQY with a small FWHM of merely 30 nm, validating the efficient energy transfer. By comparing the decay kinetics of sensitizers before and after doping (Supplementary Fig. 12), we successfully obtained FET rates (k_{FET}s) of DPT-IC → 1 wt% tCzphB-FI and 10 wt% Ir(ppy)$_2$acac → 1 wt% tCzphB-FI, being $1.0 \times 10^8\,s^{-1}$ and $8.6 \times 10^6\,s^{-1}$, respectively, as illustrated in Supplementary Table 3, 4. Both are much higher than the corresponding radiative decay rates of the sensitizers, suggesting that those multiple sensitizations could greatly accelerate exciton consumption. Moreover, the over one order-of-magnitude higher k_{FET} from TADF sensitizer can be obtained, which benefits from not only the faster radiative decay rate of TADF S$_1$ than phosphor T$_1$, but also the relatively higher concentration of DPT-IC. It is worth noting that, recently, Monkman et al. have pointed out that for efficient FET process, the kinetics of TADF sensitizer should be optimized to avoid the competition from the ISC and radiative decay processes of the sensitizer itself[44]. Here, the k_{FET} from DPT-IC singlet to that of tCzphB-FI is nearly tenfold higher than k_r and k_{ISC} of DPT-IC, suggesting a favorable energy transfer process. Moreover, a relatively long prompt lifetime of over 40 ns for DPT-IC also benefits the energy transfer process, making it a good candidate as TADF sensitizer. Moreover, we also measured the angle dependent PL spectra of tCzphB-FI in the doped film to evaluate the horizontal EDO ratio ($\Theta_{//}$) of tCzphB-FI in the doped film and a high value of 92% was obtained. This could greatly enhance the light extraction of pTSF devices for a high EQE and finally a high PE.

Electroluminescence properties of devices

OLED devices were constructed with structures of ITO/ HATCN (5 nm)/ NPB (30 nm)/ BCzPh (10 nm)/ EML (24 nm)/ 9Cz46m (10 nm)/ p-bpphen (30 nm)/ LiF (0.5 nm)/ Al (150 nm), in which HATCN was dipyrazino[2,3-f:2',3'-h]quinoxaline-2,3,6,7,10,11-hexacarbonitrile, NPB was N^4,N^4-di(naphthalen-1-yl)-N$^{4'}$,N$^{4'}$-diphenyl-[1,1'-biphenyl]-4,4'-diamine, BCzPh was 9,9'-diphenyl-9H,9'H-3,3'-bicarbazole, 9Cz46m was 4,6-bis(3-(9H-carbazol-9-yl)phenyl)pyrimidine and p-bpphen was 1,4-bis(2-phenyl-1,10-phenanthrolin-4-yl)benzene, respectively. The doped film of DPT-IC: 10 wt% Ir(ppy)$_2$acac: 1 wt% tCzphB-FI was adopted as the emitting layer (EML). For comparison, TSF and TSP devices with EMLs of DPT-IC: 1 wt% tCzphB-FI and DPT-IC: 10 wt% Ir(ppy)$_2$acac were fabricated, respectively. Figure 4a displays the corresponding energy levels of the device and the structures of the adopted molecules. The energy levels of BCzPh, DPT-IC, tCzphB-FI, Ir(ppy)$_2$acac and 9Cz46m in solid states (10 nm pristine film) were measured using LEIPS (Low Energy Inverse Photoemission Spectroscopy) for LUMOs and UPS (Ultravioletphotoelectron spectroscopy) for HOMOs, as illustrated in Supplementary Fig. 13. While the energy levels of HATCN, NPB and p-bpphen, which do not affect the charge trapping in EML, were cited from previous works[26,45]. To illustrate the charge carrier and recombination pathways, we also fabricated the corresponding single carrier devices as illustrated in Supplementary Fig. 14. Clearly, all EODs showed the similar current density, suggesting electron transport mainly through DPT-IC. On the contrary, slightly hole-trapping on

Ir(ppy)$_2$acac was observed. Considering the relatively low ratio of Ir(ppy)$_2$acac, and also the small energy barrier hole injection from BCzPh to DPT-IC, it is speculated that the main charge recombination happens on DPT-IC. Besides, the electrons on DPT-IC would also induce a strong electron electrostatic force to enhance hole injection into itself[46]. The EL decay behavior of pTSF provided below also support the main charge recombination on DPT-IC as no clear overshoot was observed after turn off of the voltage pulse, suggesting no clear charge trapping assisted recombination on the dopant.

The EL spectra of those devices were recorded at 10,000 cd/m^2 and provided in Fig. 4b. A wide green emission from Ir(ppy)$_2$acac was observed for TSP device, showing an emission peak of 525 nm, a large FWHM of 62 nm and Commission Internationale de L'Eclairage (CIE) coordinates of (0.326, 0.631), respectively. Different to the TSP device, both TSF and pTSF devices exhibited dominant sharp green emission from 2tCzphB-FI with emission peak at 532 nm and a FWHM of only 30 nm. Nevertheless, the TSF device still showed a residual weak emission from DPT-IC while the pTSF totally showed 2tCzphB-FI emission, which suggests the more efficient energy transfer in pTSF device. This can be further evidenced by EL spectra with increasing luminance as provided in Supplementary Fig. 15, showing that pTSF possessed identical spectra while the DPT-IC emission gradually enhanced for TSF devices. A corresponding CIE coordinates of (0.289, 0.684) was obtained for pTSF device, displaying a better color purity compared with the other two devices.

The luminance-voltage-current density characteristics of those three devices were provided in Fig. 4c and similar current density were observed, suggesting the similar charge recombination pathways in those three devices. Quite low operation voltages of 3.58 V at 10,000 cd/m^2 and 5.15 V at 100,000 cd/m^2 were observed for pTSF device, while those were 3.85 V and 5.82 V as well as 4.51 V and 6.76 V for TSF and TSP devices, respectively. Those low operation voltages for pTSF evidences the molecular design of DPT-IC in reducing resistive loss. Besides, a maximum luminance of up to 492,300 cd/m^2 could be achieved for pTSF while only 129,000 cd/m^2 and 209,100 cd/m^2 for TSF and TSP devices, respectively. Given the similar charge transport on the host, the difference should mainly come from the relatively higher exciton utilization for more photons in pTSF device.

Figure 4d displays the EQE-brightness-PE characteristics of those devices. A rather high maximum EQE of 39.3% was obtained for pTSF device while only 17.8% and 25.7% for TSF and TSP devices, respectively. The high EQE of pTSF device originates not only high exciton utilization efficiency but also the preferential horizontal EDO of 2tCzphB-FI as demonstrated above. The angle-dependent EL intensity of pTSF device was also measured as illustrated in Supplementary Fig. 16, which basically followed the Lambertian distribution, suggesting that the device efficiency was not overestimated. Moreover, the pTSF device showed low EQE roll-off, which remained 39.0% at 10,000 cd/m^2 and 35.4% at 100,000 cd/m^2. On the contrary, EQEs of TSF and TSP only remained 16.6% and 7.8% at 100,000 cd/m^2, respectively. For practical applications, the roll-off in efficiency with increasing luminance can be quantified by the critical luminance L$_{90\%}$, that is the luminance at which the EQE has dropped to 90% of its maximum value. An impressive L$_{90\%}$ of 97,100 cd/m^2 can be obtained for pTSF device, validating the good performance of such strategy in alleviating EQE roll-off. Owing to the combination of low operation voltage, high EQE, and narrowband spectrum, an unprecedently high maximum PE of 177.3 lm/W as obtained for pTSF device. More impressively, high PEs remained 145.1 lm/W at 10,000 cd/m^2 and 92.5 lm/W even at 100,000 cd/m^2 were observed. As comparison, only 15.1 lm/W and 33.4 lm/W were obtained for TSF and TSP devices at 100,000 cd/m^2, respectively. The alleviated PE roll-off for pTSF device should be assigned to its not only the alleviated EQE roll-off but also the small energy loss and resistive loss with the increased luminance. The device operation stabilities of those devices were also testified
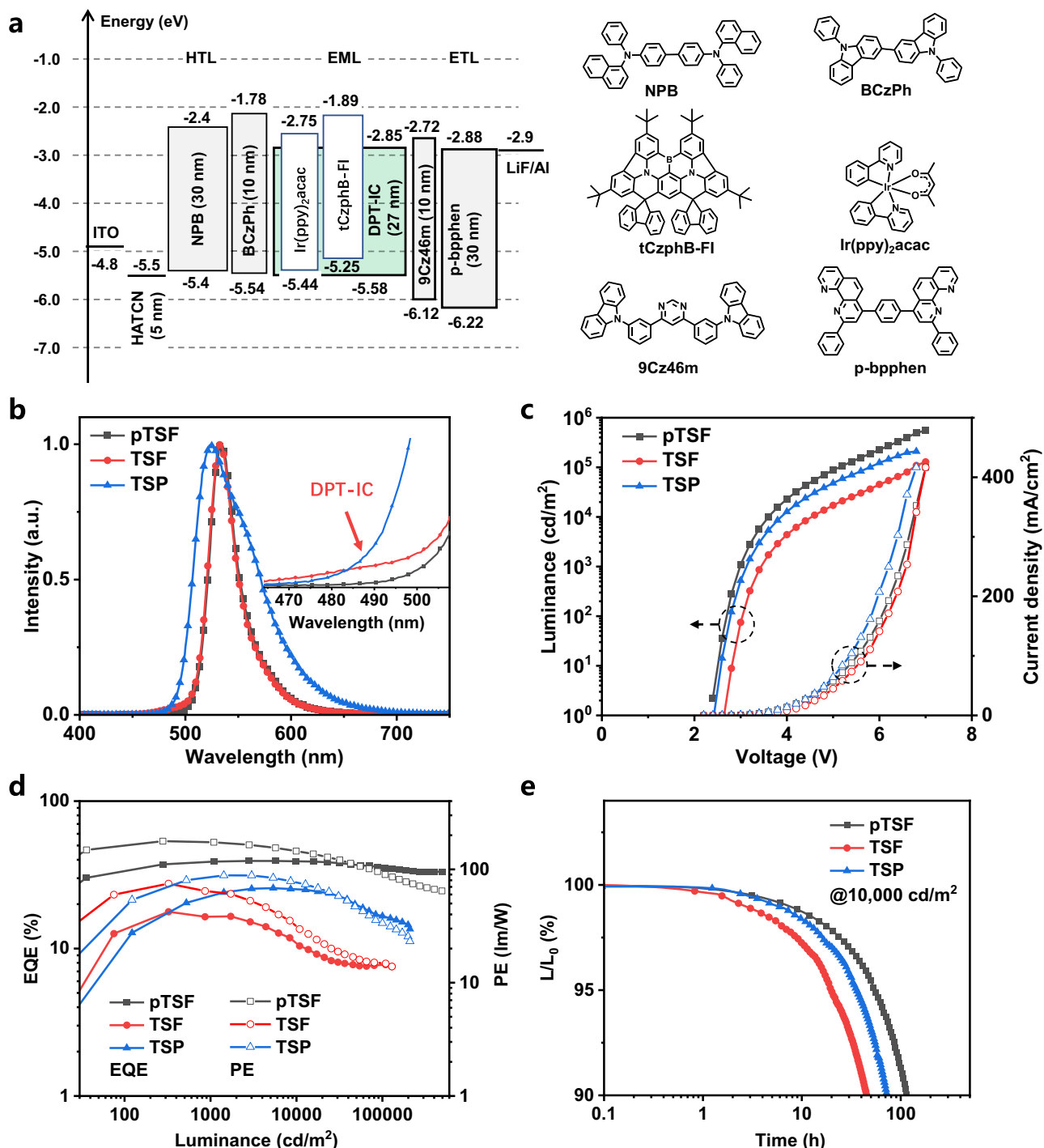
Fig. 4 | Device performance characterizations. a The energy level structure of the device and the molecular structures of the adopted compounds. **b** The EL spectra of those devices taken at 10,000 cd/m². **c** The luminance-voltage-current density curves of those devices. **d** The EQE-luminance-PE characteristics. **e** Normalized luminance of those devices as a function of operating time at a constant current density with the initial luminance of 10,000 cd/m².

under a constant current density with a L_0 of 10,000 cd/m². Figure 4e illustrated the relative luminance of those devices as a function of operation times. The pTSF device showed a LT90 of 114 h, significantly longer than the TSF and TSP devices, which only achieved a value of 45 h and 76 h, respectively. Those results greatly validated our inspiration that by wisely designing the TADF sensitizing host, an OLED based on the pTSF emission could unlock the full potential PE under high luminance and enhance device operation stability at the meantime.

To unveil the performance differences of those devices, the EL transient decay behaviors were monitored at the dominant emission peaks under the same voltage of 4 V and the results were illustrated in Fig. 5a. For TSP device, a single-exponential curve was observed with a fitted decay lifetime of 0.897 μs, in agreement with the typical excited state lifetime of phosphorescence emission from Ir(ppy)₂acac. For TSF device, after a short-lived but low ratio prompt part due to the energy transfer from the direct charge recombination generated TADF singlet to the MR emitter, a long-lived delayed tail with a main ratio was
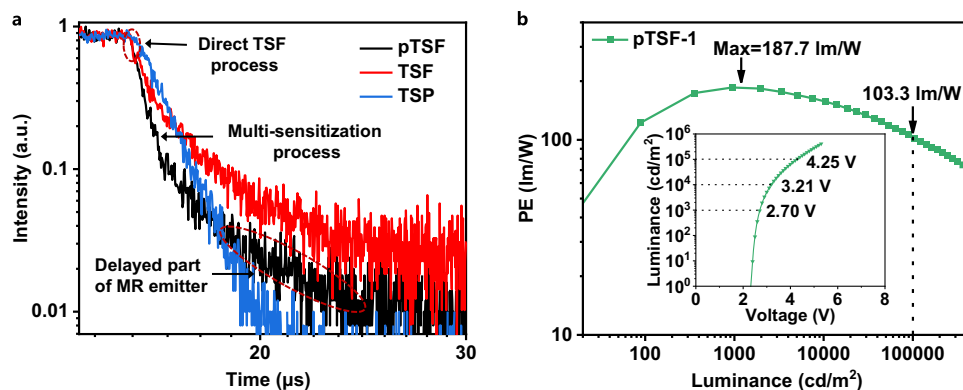
Fig. 5 | EL decay behaviors and device performances of pTSF−1. a The transient decay curves of those devices. **b** The PE-luminance characters of pTSF−1 and the inserted figure is its luminance-voltage character.

observed, which is even longer than TSP device and thus should account for its most severe efficiency roll-off. The delayed component should mainly originate from the singlet-to-triplet cycle on the TADF host induced by the ISC process as we discussed above. In terms of the pTSF devices, a clearly short-lived decay curve was observed compared with both TSF and TSP devices. Considering the high EQE of pTSF device, the influence of the nonradiative decay process could be ruled out and the short decay lifetime mainly arise from the accelerated exciton radiative consumption. The reasons of both efficiency roll-off and device degradation have been convincingly assigned to the exciton related annihilations, which leads to exciton loss and also molecular dissociation. The short-lived excitons in pTSF device could reduce the exciton concentrations under high luminance to decrease the possibility of exciton annihilations, thus explaining the alleviated efficiency roll-off and the prolonged device operation stability also.

To be more specific, a multi-exponential character was observed for the decay curve of the pTSF device, suggesting its multiple exciton radiative consumption channels. Initially, a fast decay component overlapping with the prompt part of the TSF device was observed, suggesting the direct TSF process. After that, the pTSF device exhibited a faster decay part compared with the TSF device, of which the reason is attributed to the additional sensitization process assisted by the phosphor as aforementioned. Those decay behaviors validated the existence of the multiple sensitization processes in the pTSF device. What needs to point out is that a long tail was also recorded for pTSF, which is even longer than TSP devices. The reason should be attributed to the slow TADF process of MR emitter itself. Even if the sensitization process could initially generate 100% S_1 on the final emitter, the ISC process of MR molecule still leads to the formation of its T_1 and then participate in the succedent RISC process, which, however, is dynamically slow (rate constant of usually ~10^3–$10^4 s^{-1}$). Fortunately, the ratio of the long tail is relatively low (<10%) and the decay lifetime is still much shorter than TSF device, lowering down the influence on efficiency roll-off.

Furthermore, considering the fact that the EML of pTSF device showed a relatively better electron transporting than the hole one according to the single carrier devices (Supplementary Fig. 14e), we optimized the EML structure by introducing 30 wt% BCzPh to construct a pTSF-1 device with an EML of DPT-IC: 30 wt% BCzPh: 10 wt% Ir(ppy)$_2$acac:1 wt% 2tCzphB-FI (Supplementary Fig. 17), aiming to enhance hole transporting to further lower the driving voltage and balance charges (evidenced by Supplementary Fig. 14f). It should also be pointed out that, the dilute DPT-IC by BCzPh should show a relatively higher PLQY compared with the pristine ones as illustrated by Supplementary Fig. 8, which may slightly affect the energy transfer process in the device. As illustrated in Fig. 5b, Table 1 and

Supplementary Fig. 17b, a low voltage of 4.25 V at 100,000 cd/m^2 was recorded for pTSF-1, being 0.90 V lower than the above pTSF device, evidencing the small resistive loss with increasing luminance. To the best of our knowledge, this operation voltage represents the lowest one among the green OLEDs with common device structures in literature and it is even comparable with or better than the cutting-edge perovskite LEDs and polaritonic OLEDs, which are well-known for their low operation voltages[29–31]. This device also showed nearly roll-off-free EQE as illustrated in Supplementary Fig. 17c with a maximum value of 36.1%, which remained 33.3% at 100,000 cd/m^2. Recently, Samuel and Zysman-Colman et al. have summarized and analyzed the EQE roll-off of OLEDs using $J_{90\%}$ as the yardstick and a high $J_{90\%}$ of ~65 mA/cm^2 was observed for the pTSF-1 device (Supplementary Fig. 17d). This value outperforms nearly all TADF and phosphorescent devices and is comparable with the best fluorescence ones but with nearly three-fold higher EQE value as summarized in Supplementary Fig. 17e, evidencing the greatly alleviated roll-off in EQE together with high absolute values[28]. This naturally should benefit from the fast exciton consumption and the excellent charge transport ability of pTSF-1 device. Combining with the high EQE and small resistive loss, a state-of-the-art PE with a maximum value of 187.7 lm/W was therefore obtained, which remained 158.0 lm/W and 103.3 lm/W at 10,000 cd/m^2 and 100,000 cd/m^2, respectively. More impressively, an high $L_{PE=100\ lm/W}$ of 114,330 cd/m^2 was obtained, nearly one order of magnitude higher than previous works as illustrated in Fig. 1a. The device operation stability was also testified under a constant current density with a L_0 of 10,000 cd/m^2 and a long LT90 of 135 h was recorded as depicted in Supplementary Fig. 17f, suggesting the good stability of pTSF-1.

Discussion

In this manuscript, we demonstrated the strategic implementation of a pTSF narrowband emission aiming to break the trade-off between a high luminance and a high PE for OLEDs. On one hand, the multiple sensitization channels in pTSF system could greatly accelerate the exciton consumption to achieve a 100% exciton radiative consumption with decay times mainly in the sub-microsecond regime, thus suppressing the EQE roll-off induced by exciton annihilation under high brightness. On the other hand, the adoption of MR emitter in pTSF system was in consideration of a narrowband spectrum but also a small stokes shift, guaranteeing efficient energy transfer from both TADF sensitizing-host and phosphor-assistant with nearly energetically similar spectra, which could reduce the energetic losses during the energy transfer. Moreover, the common donor-acceptor architecture of TADF sensitizing-host with small ΔE_{ST} benefit not only bipolar charge transport but also small energy barriers with the adjacent transport layers in the prerequisite of a high enough triplet states, reducing resistive loss with increasing luminance. Therefore, this pTSF

Table 1 | Summary of the device performances

Device	Maximum		10,000 cd/m²			100,000 cd/m²			LT90[a]	CIE(x,y)
	EQE (%)	PE (lm/W)	Voltage (V)	EQE (%)	PE (lm/W)	Voltage (V)	EQE (%)	PE (lm/W)		
pTSF	39.3	177.3	3.58	39.0	145.1	5.15	35.4	92.5	114	(0.289, 0.684)
TSP	25.7	88.5	3.85	25.3	77.0	5.82	16.6	33.4	76	(0.326, 0.631)
TSF	17.8	74.8	4.51	11.0	32.3	6.76	7.8	15.1	45	(0.280, 0.679)
pTSF–1	36.1	187.7	3.21	37.8	158.0	4.25	33.3	103.3	135	(0.289, 0.684)

[a]Testified under a constant current density with an initial luminance of 10,000 cd/m².

emission could potentially satisfy all the requirements for a high PE with increasing luminance.

The key to maximize the performance of pTSF system is a dedicated designed TADF sensitizing-host. With this in mind, an ortho-linked donor-dual-acceptor architecture TADF molecule was developed in our work, which possessed a fast reverse ISC benefiting from multiple degenerate states, an anti-aggregation caused quenching character, a bipolar charge transport ability and moderate energy levels simultaneously. Based on this host, the corresponding pTSF device exhibited a narrowband EL spectrum with a small FWHM of 30 nm, a high external quantum efficiency of 33.3% and a low operating voltage of 4.25 V recorded at 100,000 cd/m² simultaneously. As a result, not only a large PE$_{max}$ of 187.7 lm/W was achieved, but also a truly remarkable high L$_{PE=100\ lm/W}$ of over 110,000 cd/m², almost ten times higher than the previous record. Moreover, a long LT90 of 135 h at a L$_0$ of 10,000 cd/m² was also obtained, suggesting the good operation stability of this device.

Taking the influence of the slow TADF property of MR emitters into consideration as observed in the EL decay, the roll-off in PE could be further suppressed by either strongly enhancing the TADF process of MR emitter or totally eliminating influence of ISC process by enlarging its ΔE_{ST} to make it a non-TADF but narrowband emission fluorophore. Furthermore, given that EQE is also limited by the plate structure of OLEDs, it is believed that the value of PE could be further improved by enhancing light extraction. Our work would be insightful for the rationally design of OLEDs in high-luminance required applications including white lighting illuminations, transparent displays or even electrically pumped organic semiconductor laser diodes and so on.

Methods

General information

All the commercially available reagents were used as received and all the measurements were carried out at RT unless otherwise stated. The reagents for the synthesis of DTP-IC were mainly purchased from Shanghai Bide Medical Technology Co. Ltd. The compounds used in the device were purchased from Jilin Optical and Electronic Materials Co. Ltd. The final emitter, tCzphB-FI, was synthesized according to the literature[43]. The reactions of the synthetic procedure were carried out under a nitrogen atmosphere using Schlenk techniques. For the ¹H NMR spectrum measurement of DPT-IC, a JEOL JNM-ECS600 spectrometer (600 Hz) was adopted, with the compound dissolved in in deuterated dichloromethane with tetramethyl silane as the internal standard. The molecular mass was measured using Matrix-Assisted Laser Desorption/Ionization Time of Flight Mass Spectrometry (MALDI-TOF-MS) with a Shimadzu AXIMA Performance MALDI-TOF instrument in positive detection modes.

Analysis of single-crystal structure

The diffraction data of single crystal of DPT-IC was collected using a Rigaku R-AXIS-RAPID diffractometer at the ω-scan mode with graphite-monochromator Mo•Kα radiation. And the SHELXTL programs was used to directly determine the molecular structure, which was further refined using full-matrix least squares on F2. The data could be obtained freely from the Cambridge Crystallographic Data Centre via www.ccdc.cam.ac.uk/data_request/cif with a CCDC reference number of 2355309. The crystal data and structure refinement for DPT-IC has been provided in Supplementary Table 5.

Computational methods

The electronic properties of the molecular in the ground state were studied performed with the Gaussian 16 package using the density functional theory (DFT) and excited-state electronic analysis by TD-DFT method with the same basis of B3LYP/6-31(G)*[47]. The Multiwfn program was adopted to calculate the RDG, which was then plotted by VMD[48,49]. The hole-particle analysis of the degenerate singlet and triplet states was conducted using the Multiwfn 3.8 program and the SOCME values between those states were calculated with ORCA package[50]. The cartesian coordinate of DPT-IC (S$_0$) has been provided in Supplementary Table 6.

Photophysical property measurements

The solutions with concentration of 1×10^{-5} M were prepared for the solution measurements. All the organic films used for the photoluminescence measurements were deposited onto clean quartz substrates by thermal evaporation at 1–1.5 Å s⁻¹ under high vacuum with a base pressure of <10⁻⁶ torr. An Agilent 8453 spectrophotometer was used for the UV-vis absorption spectra measurement while a Hitachi F-7000 Fluorescence Spectrometer for the steady fluorescence and phosphorescence spectra. Edinburgh fluorescence spectrometer (FLS1000) using picosecond pulsed diode laser was adopted to measure the photoluminescence decay curve under an excitation wavelength at 375 nm. And a Hamamatsu absolute PL quantum yield spectrometer (C9920-02G) with an integrating sphere was used for the photoluminescence quantum yields measurement.

The rate constants of TADF process were calculated using the equations below[51]:

$$k_r = \frac{\Phi_{PF}}{\tau_{PF}} \tag{1}$$

$$k_{ISC} = \frac{1 - \Phi_{PF}}{\tau_{PF}} \tag{2}$$

$$k_{RISC} = \frac{\Phi_{DF}}{\tau_{DF} k_{ISC} \tau_{PF} \Phi_{PF}} \tag{3}$$

The FET radii was calculated by equation[44]:

$$R_0^6 = \frac{9000 \ln 10}{128 \pi^5 n^4 N_A} \eta_{PL} \kappa^2 \int_0^\infty f_D(\lambda) \varepsilon_A(\lambda) \lambda^4 d\lambda \tag{4}$$

R_O is the distance between D and A. κ^2 is the azimuth factor, usually 2/3. N_A is AvogadLuo constant. n is the material refractive index, for organic materials generally 1.7. $\int_0^\infty f_D(\lambda)\varepsilon_A(\lambda)\lambda^4 d\lambda$ is the overlap integral between the emission spectrum of D and the absorption spectrum of A.

A RSQX-01 instrument (Changchun Ruoshui Co.) was adopted to measure the horizontal emitting dipole ratio (Θ) of the final emitter doped in a 30-nm-thick film fabricated by thermal vacuum evaporation onto a D-shape quartz column substrate. A continuous-wave laser was used as the excitation source with an excitation wavelength of 360 nm and a fixed excitation angle of 45°. The photoluminescence intensity with varied angles were recorded at the peak wavelength of the film as the sample stage was rotated automatically at intervals of 3° from −3° to 90°. The wavelength range is between 380 nm and 800 nm.

The FET rate can be calculated using a method previous reported[36], based on the comparison of the decay kinetics of sensitizers (energy donor) before and after the introduction of the final emitter (the energy acceptor). The k_{FET} can be calculated using the equation below:

$$k_{FET} = \frac{1}{\tau_{sensitizer}} - \frac{1}{\tau_{sensitizer-dopant}} \tag{5}$$

For a TADF sensitizer, $\tau_{sensitizer}$ and $\tau_{sensitizer-dopant}$ stands for the prompt lifetime of sensitizer before and after doping. For a phosphorescence sensitizer, $\tau_{sensitizer}$ and $\tau_{sensitizer-dopant}$ stands for the triplet radiative lifetime of sensitizer before and after doping.

Electrochemical and thermal stability measurements
A Potentiostat/Galvanostat Model 283 (Princeton Applied Research) electrochemical workstation was used for the electrochemical measurements with Pt as the working electrode, platinum wire as the auxiliary electrode, and an Ag wire as the reference electrode standardized against ferrocene/ferrocenium. A concentration of 10 mg/mL for DPT-IC and a scan rate of 100 mV s^{-1} were adopted during the measurement. The dichloromethane (CH_2Cl_2) solution using 0.1 M n-Bu$_4$NPF$_6$ as the supporting electrolyte was used for the oxidation potential measurement while N, N-Dimethylformamide (DMF) solution containing 0.1 M n-Bu$_4$NClO$_4$ for the reduction potentials. The TGA of DPT-IC was measured using TGA55 (TA Instrument) with a temperature range from 30 to 600 °C and a heating rate of 10 °C/min. The LUMO and LUOMO energy levels were determined from the cathodic reduction and oxidation potentials, respectively. The UPS (Ultravioletphotoelectron spectroscopy) measurement was carried out by an Axis Ultra DLD (Kratos, UK) spectrometer with a He-I (21.21 eV) excitation source and a pass energy of 5 eV. A bias voltage of −9 V was applied to the sample during measurement for obtaining the cut-off region of secondary electrons. The Fermi level was identified by using Au as a reference. The LEIPS (Low Energy Inverse Photoemission Spectroscopy) measurement was performed on a customized ULVAC-PHI LEIPS instrument with Bremsstrahlung isochromatic mode.

OLED fabrication and characterization
All the compounds for the device fabrication were firstly subjected to temperature-gradient sublimation under high vacuum. The ITO-coated transparent glass was adopted as the substrates for OLEDs with multiple organic functional layers sandwiched between the bottom ITO anode and the top metal cathode. The substrates were pre-cleaned carefully before device fabrication and the functional films were then deposited by evaporation in a vacuum chamber with a base pressure of 10^{-6} torr. The complete device was fabricated in a single vacuum pump-down without breaking vacuum to guarantee device performances. For the organic films, a deposition rate of 1.0 Å s^{-1} was maintained. The doping ratio in emitting layer was conducted by co-evaporation from the corresponding separated evaporation sources with different evaporation rates. The device was finally encapsulated before characterization. An EQE measurement system (Hamamatsu C9920-12, equipped with Hamamatsu PMA-12 Photonic multichannel analyzer C10027-02 whose longest detection wavelength is 1100 nm) integrating with a Keithley 2400 source meter was used to characterize the EL performances of the devices, including the current density, voltage, luminance, EQE, electroluminescent spectra and other EL properties at the same time. The angle-dependent EL intensity of pTSF device was measured using Hamamatsu C9920-11 system under a constant voltage of 4 V with the anlge range was set from 0° to ±90° with a step of 5°. The EL decay behaviors were detected sing an Edinburgh FLS1000 transient spectrometer with the device being excited by a short-pulse generated by an Agilent 8114 A. The short-pulse possesses a pulse width of 15 μs, an amplitude of 7 V and a baseline of -3 V, respectively. The whole period was 50 μs with a delayed time 25 μs and a duty cycle 30%. The device operation lifetimes were measured using an OLED aging lifetime tester (ZJZCL-1, Shanghai University). Measurements were taken in a standard laboratory with a RT around 20 °C–30 °C and a humidity of 20–40%.

Data availability
The data generated in this study are provided in the Supplementary Information/Source Data file. Crystallographic data for the structures reported in this Article have been deposited at the Cambridge Crystallographic Data Centre, under deposition numbers 2355309. Copies of the data can be obtained free of charge via https://www.ccdc.cam.ac.uk/structures/. Source data are provided with this paper.

References
1. Fyfe, D. Organic displays come of age. *Nat. Photon* **3**, 453–455 (2009).
2. Huang, Y. et al. Mini-LED, micro-LED and OLED displays: present status and future perspectives. *Light Sci. Appl.* **9**, 105 (2020).
3. Hong, G. et al. A brief history of OLEDs-emitter development and industry milestones. *Adv. Mater.* **33**, 2005630 (2021).
4. Reineke, S. et al. White organic light-emitting diodes with fluorescent tube efficiency. *Nature* **459**, 234–238 (2009).
5. Baldo, M. et al. Highly efficient phosphorescent emission from organic electroluminescent devices. *Nature* **395**, 151–154 (1998).
6. Zhang, Y., Lee, J. & Forrest, S. Tenfold increase in the lifetime of blue phosphorescent organic light-emitting diodes. *Nat. Commun.* **5**, 5008 (2014).
7. Uoyama, H., Goushi, K., Shizu, K., Nomura, H. & Adachi, C. Highly efficient organic light-emitting diodes from delayed fluorescence. *Nature* **492**, 234–238 (2012).
8. Kaji, H. et al. Purely organic electroluminescent material realizing 100% conversion from electricity to light. *Nat. Commun.* **6**, 8476–8484 (2015).
9. Wu, T.-L. et al. Diboron compound-based organic light-emitting diodes with high efficiency and reduced efficiency roll-off. *Nat. Photonics* **12**, 235–240 (2018).
10. Kim, S.-Y. et al. Organic light-emitting diodes with 30% external quantum efficiency based on a horizontally oriented emitter. *Adv. Funct. Mater.* **23**, 3896–3900 (2013).
11. Shih, C.-J. et al. Versatile exciplex-forming co-host for improving efficiency and lifetime of fluorescent and phosphorescent organic light-emitting diodes. *ACS Appl. Mater. Interfaces* **10**, 24090–24098 (2018).
12. Wu, Z. et al. Precise exciton allocation for highly efficient white organic light-emitting diodes with low efficiency roll-off based on blue thermally activated delayed fluorescent exciplex emission. *Adv. Opt. Mater.* **5**, 1700415 (2017).
13. Wu, S.-F. et al. White organic LED with a luminous efficacy exceeding 100 lm W^{-1} without light out-coupling enhancement techniques. *Adv. Funct. Mater.* **27**, 1701314 (2017).

14. Kumar, A. et al. Triarylboron-based TADF emitters with perfluoro substituents: high-efficiency OLEDs with a power efficiency over 100 lm W−1. *J. Mater. Chem. C* **8**, 4253–4263 (2020).

15. Tanaka, D. et al. Ultra high efficiency green organic light-emitting devices. *Jpn J. Appl. Phys.* **46**, L10 (2007).

16. Kim, K.-H., Moon, C.-K., Lee, J.-H., Kim, S.-Y. & Kim, J.-J. Highly efficient organic light-emitting diodes with phosphorescent emitters having high quantum yield and horizontal orientation of transition dipole moments. *Adv. Mater.* **26**, 3844–3847 (2014).

17. Seino, Y., Inomata, S., Sasabe, H., Pu, Y.-J. & Kido, J. High-performance green OLEDs using thermally activated delayed fluorescence with a power efficiency of over 100 lm W−1. *Adv. Mater.* **28**, 2638–2643 (2016).

18. Chen, C.-H. et al. New bipolar host materials for high power efficiency green thermally activated delayed fluorescence OLEDs. *Chem. Eng. J.* **442**, 136292 (2022).

19. Sasabe, H. et al. Ultrahigh power efficiency thermally activated delayed fluorescent OLEDs by the strategic use of electron-transport materials. *Adv. Opt. Mater.* **6**, 1800376 (2018).

20. Zhang, D., Qiao, J., Zhang, D. & Duan, L. Ultrahigh-efficiency green PHOLEDs with a voltage under 3 V and a power efficiency of nearly 110 lm W−1 at luminance of 10,000 cd m−2. *Adv. Mater.* **29**, 1702847 (2017).

21. Hu, Y. X. et al. Efficient selenium-integrated TADF OLEDs with reduced roll-off. *Nat. Photonics* **16**, 803–810 (2022).

22. Wang, J. et al. Metal-perturbed multiresonance TADF emitter enables high-efficiency and ultralow efficiency roll-off non-sensitized OLEDs with pure green gamut. *Adv. Mater.* **35**, 2208378 (2023).

23. Park, Y.-S. et al. Exciplex-forming co-host for organic light-emitting diodes with ultimate efficiency. *Adv. Funct. Mater.* **23**, 4914–4920 (2013).

24. Zhang, Y.-L., Ran, Q., Wang, Q., Fan, J. & Liao, L.-S. High-efficiency exciplex-based white organic light-emitting diodes with a new tripodal material as a co-host. *J. Mater. Chem. C* **7**, 7267–7272 (2019).

25. Kawano, T. et al. Tetrapyridine/triphenyltriazine-conjugated electron transporters for low-power-consumption, high-stability phosphorescent OLEDs. *J. Mater. Chem. C* **11**, 4129–4135 (2023).

26. Chen, Y. et al. Approaching nearly 40% external quantum efficiency in organic light emitting diodes utilizing a green thermally activated delayed fluorescence emitter with an extended linear donor-acceptor-donor structure. *Adv. Mater.* **33**, 2103293 (2021).

27. Murawski, C., Leo, K. & Gather, M. C. Efficiency roll-off in organic light-emitting diodes. *Adv. Mater.* **25**, 6801–6827 (2013).

28. Yin, C. et al. Highly efficient and nearly roll-off–free electro-fluorescent devices via multiple sensitizations. *Sci. Adv.* **8**, eabp9203 (2022).

29. Diesing, S. et al. A figure of merit for efficiency roll-off in TADF-based organic LEDs. *Nature* **627**, 747–753 (2024).

30. Ding, S. et al. Phase dimensions resolving of efficient and stable perovskite light-emitting diodes at high brightness. *Nat. Photonics* **18**, 363–370 (2024).

31. Kim, J. S. et al. Ultra-bright, efficient and stable perovskite light-emitting diodes. *Nature* **611**, 688–694 (2022).

32. Mischok, A. et al. Highly efficient polaritonic light-emitting diodes with angle-independent narrowband emission. *Nat. Photonics* **17**, 393–400 (2023).

33. Wang, S. M. et al. Towards high-power-efficiency solution-processed OLEDs: Material and device perspectives. *Mat. Sci. Eng. R.* **140**, 100547 (2020).

34. Vandersteegen, P., Schwartz, G., Bienstman, P. & Baets, R. Luminous power efficiency optimization of a white organic light-emitting diode by tuning its spectrum and its extraction efficiency. *Appl. Opt.* **47**, 1947–1955 (2008).

35. Nakanotani, H. et al. High-efficiency organic light-emitting diodes with fluorescent emitters. *Nat. Commun.* **5**, 4016 (2014).

36. Zhang, D. D. et al. High-efficiency fluorescent organic light-emitting devices using sensitizing hosts with a small singlet–triplet exchange energy. *Adv. Mater.* **26**, 5050–5055 (2014).

37. Zhang, D. D., Song, X. Z., Cai, M. H. & Duan, L. Blocking energy-loss pathways for ideal fluorescent organic light-emitting diodes with thermally activated delayed fluorescent sensitizers. *Adv. Mater.* **30**, 1705250 (2018).

38. Kim, K. H. & Kim, J. J. Origin and control of orientation of phosphorescent and TADF dyes for high-efficiency OLEDs. *Adv. Mater.* **30**, 1705600 (2018).

39. Min, H., Park, I. S. & Yasuda, T. Blue thermally activated delayed fluorescence with sub-microsecond short exciton lifetimes: acceleration of triplet–singlet spin interconversion via quadrupolar charge-transfer states. *Adv. Opt. Mater.* **10**, 2200290 (2022).

40. Yin, C. et al. High-efficiency narrow-band electro-fluorescent devices with thermally activated delayed fluorescence sensitizers combined through-bond and through-space charge transfers. *CCS Chem.* **2**, 1268–1277 (2020).

41. Tang, X. et al. Highly efficient luminescence from space-confined charge-transfer emitters. *Nat. Mater.* **19**, 1332–1338 (2020).

42. Crovini, E. et al. Molecular geometry and the photophysics of thermally activated delayed fluorescence: the strange case of DMAC-py-TRZ. *J. Mater. Chem. C.* **11**, 8284–8292 (2023).

43. Liu, J. et al. Toward a BT.2020 green emitter through a combined multiple resonance effect and multi-lock strategy. *Nat. Commun.* **13**, 4876 (2022).

44. Stavrou, K. et al. Key requirements for ultraefficient sensitization in hyperfluorescence organic light-emitting diodes. *Nat. Photon* **18**, 554–561 (2024).

45. Kim, G. W. et al. Diphenanthroline electron transport materials for the efficient charge generation unit in tandem organic light-emitting diodes. *Chem. Mater.* **29**, 8299–8312 (2017).

46. Jou, J. et al. Highly efficient orange-red phosphorescent organic light-emitting diode using 2,7-bis(carbazo-9-yl)-9,9-ditolyfluorene as the host. *Appl. Phys. Lett.* **96**, 143306 (2010).

47. Frisch, M. J. et al. Gaussian 16, Revision C.01 (Gaussian, Inc., Wallingford, CT, 2016).

48. Lu, T. & Chen, F. Multiwfn: a multifunctional wavefunction analyzer. *J. Comput. Chem.* **33**, 580–592 (2012).

49. Humphrey, W., Dalke, A. & Schulten, K. VMD: visual molecular dynamics. *J. Mol. Graph.* **14**, 33–38 (1996).

50. Neese, F. The ORCA program system. *WIREs Comput. Mol. Sci.* **2**, 73–78 (2012).

51. Masui, K., Nakanotani, H. & Adachi, C. Analysis of exciton annihilation in high-efficiency sky-blue organic light-emitting diodes with thermally activated delayed fluorescence. *Org. Electron.* **14**, 2721–2726 (2013).

Acknowledgements

Author contributions

D.Z. supervised the project, conceived the conceptual idea and designed the experiments. C.Y. and Y.X. synthesized and characterized the TADF sensitizing-host material. C.Y. performed the theoretical calculations, photophysical characterization, OLED fabrication, and measurement. T.H. helped with the theoretical calculation. Y.X. carried out the measurement of the molecular dipolar orientation and helped the device fabrication experiments. Q.Z. provided suggestions on

experiments and revised the manuscript. D.Z. and L.D. analyzed the results and wrote the manuscript.

Competing interests

The authors declare no competing interests.

Additional information

Supplementary information The online version contains supplementary material available at https://doi.org/10.1038/s41467-024-55564-5.

Correspondence and requests for materials should be addressed to Dongdong Zhang.

Peer review information *Nature Communications* thanks Zujin Zhao, Kleitos Stavrou, and the other, anonymous, reviewer(s) for their contribution to the peer review of this work. A peer review file is available.

Reprints and permissions information is available at http://www.nature.com/reprints